

Disorder-enhanced subwavelength phenomena in thin elastic solids with heterogeneously tuned resonators

Paolo Celli* and Stefano Gonella†

*Department of Civil, Environmental, and Geo- Engineering,
University of Minnesota, Minneapolis, MN 55455, USA*

*pcelli@umn.edu, †sgonella@umn.edu

October 1, 2022

In this letter, we report on a family of subwavelength wave manipulation effects experimentally observed in metamaterial plates endowed with heterogeneous populations of tunable resonators. We first document effects in terms of wave attenuation, resulting from the interplay between disorder and heterogeneity, illustrating how random spatial arrangements outperform functionally-graded architectures in terms of achievable total bandgap width. We then proceed to demonstrate the onset of subwavelength localization phenomena—whose manifestation is marked by an unconventional bandgap “push-up” that appears to be germane to the problem of elastic wave propagation. To agilely explore the effects of a broad spectrum of architectural modifications on the wave response, we resort to modular stubbed plate specimens, featuring spatially rearrangeable and manually tunable telescopic resonators.

Due to their peculiar mesoscale architectures, metamaterials are capable of attenuating [1], anomalously refracting [2], focusing [3], cloaking [4], imaging [5], trapping [6] and guiding [7] waves in the *subwavelength* regime—when the wavelengths are much larger than the characteristic microstructural length scales of the medium. Some of these effects, like subwavelength waveguiding and rainbow trapping, require the coexistence of *heterogeneous* populations of resonators. For example, subwavelength waveguiding (where the waveguide width is the characteristic length scale) has been achieved by carving a path of defects in a medium featuring periodically-placed resonators, and by placing up-shifted resonators along the defected path [7–10]. Similarly, rainbow trapping requires arrays of resonators with functionally graded characteristics, where each resonator distills a selected frequency from a broadband input signal [6, 11–15].

Inspired by recent developments in electromagnetics and acoustics, we set forth to investigate subwavelength phenomena in the realm of elastodynamics, where interesting effects result from the combined action of the heterogeneity of the resonators, their spatial organization, and the mechanical coupling between them. We choose as wave-carrying medium a stubbed plate (a thin sheet with pillar resonators [16–24]), and we show how the already broadband attenuation characteristics displayed by configurations featuring functionally-graded distributions of resonators can be systematically improved by spatially randomizing the pillar arrangement (and establishing favorable conditions for the onset of Anderson localization mechanisms [25]). Additionally, we deploy sets of up-shifted resonators (whose resonance falls within, or after, the bandgap of the dominant population of resonators) in selected subre-

gions of the specimens, to elicit manifestations of subwavelength localization phenomena that appear to be germane to the elastic wave regime.

In order to achieve the versatility required to test multiple architectures within a single reconfigurable specimen, we assemble a modular stubbed plate with *telescopic* resonators. The desired modularity [26–28] is achieved using a flexible fabrication framework, inspired by our previous experimental work [24], which involves the arrangement of arrays of LEGO® bricks on a thin baseplate. Here, as shown in Fig. 1, each resonator consists of a rod and a con-

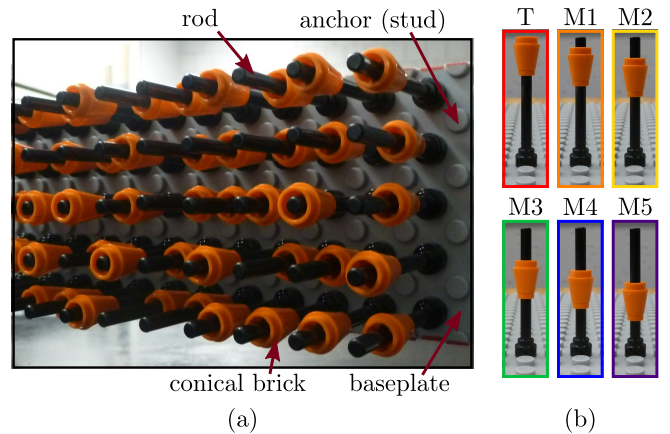


FIGURE 1: (a) Detail of a stubbed plate specimen. (b) Families of resonators (from T to M5) obtained using a single telescopic pillar element by sliding the conical brick down the rod by discrete increments.

ical brick, and can be tuned by sliding the brick up and down, thus altering its inertial characteristics and its natural frequencies. This tuning strategy is conceptually similar

to those discussed by other authors for Bragg bandgap tunability [29–31].

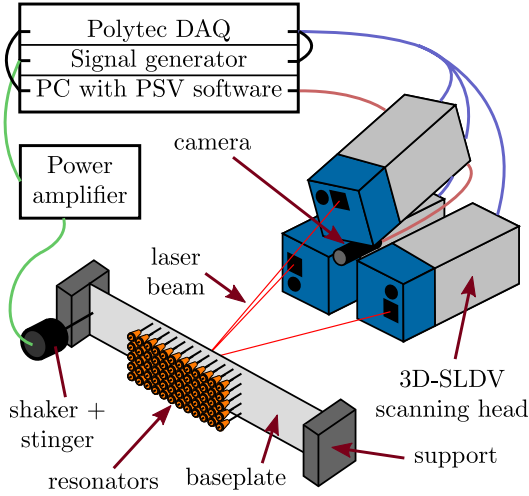


FIGURE 2: Schematic of the experimental setup.

Our experimental setup is schematically illustrated in Fig. 2. The specimen (a detail of which is shown in Fig. 1a) consists of a long strip cut out of a baseplate and features an array of telescopic resonators arranged in a square lattice. The resonators can assume one of the six quantized inertial configurations shown in Fig. 1b, obtained by sliding the conical brick down the rod by discrete increments (3.25 mm). Each configuration is color coded and this coding is used to visually illustrate how the bricks are spatially arranged in each experiment. The metamaterial plates are probed with a pseudorandom waveform to analyze standing wave patterns over a broad spectrum of frequencies, and their response is recorded with a 3D Scanning Laser Doppler Vibrometer (3D-SLDV). We use two almost identical setups, which only differ from each other by slightly different boundary conditions: the first setup is used throughout the bandgap analysis, while the second one is used for the subwavelength localization experiments. More details are discussed in the Supplemental Material section [32].

Locally resonant bandgaps are narrow-banded in nature. This limitation has inspired numerous corrective (widening) strategies, among which we recall trampoline effects [33], rainbow trapping [12], bandgap adjoining [34, 35], and disorder-based methods based on Anderson localization arguments [36, 37]. Here, we specifically investigate the dependence of the bandgap width upon the order (or lack thereof) attributes of heterogeneous populations of resonators—de facto combining the requirements for rainbow trapping and Anderson localization effects in a single experiment. To this end, we perform a transmissibility analysis as shown in Fig. 3. Each subfigure comprises several superimposed transmissibility plots, obtained for different architectures by plotting $v_{z,ave}^{out}/v_{z,ave}^{in}$, where $v_{z,ave}^{in}$ is the average out-of-plane velocity spectrum at points near the wave source and $v_{z,ave}^{out}$ is the same quantity measured away from the source (near the opposite support). The

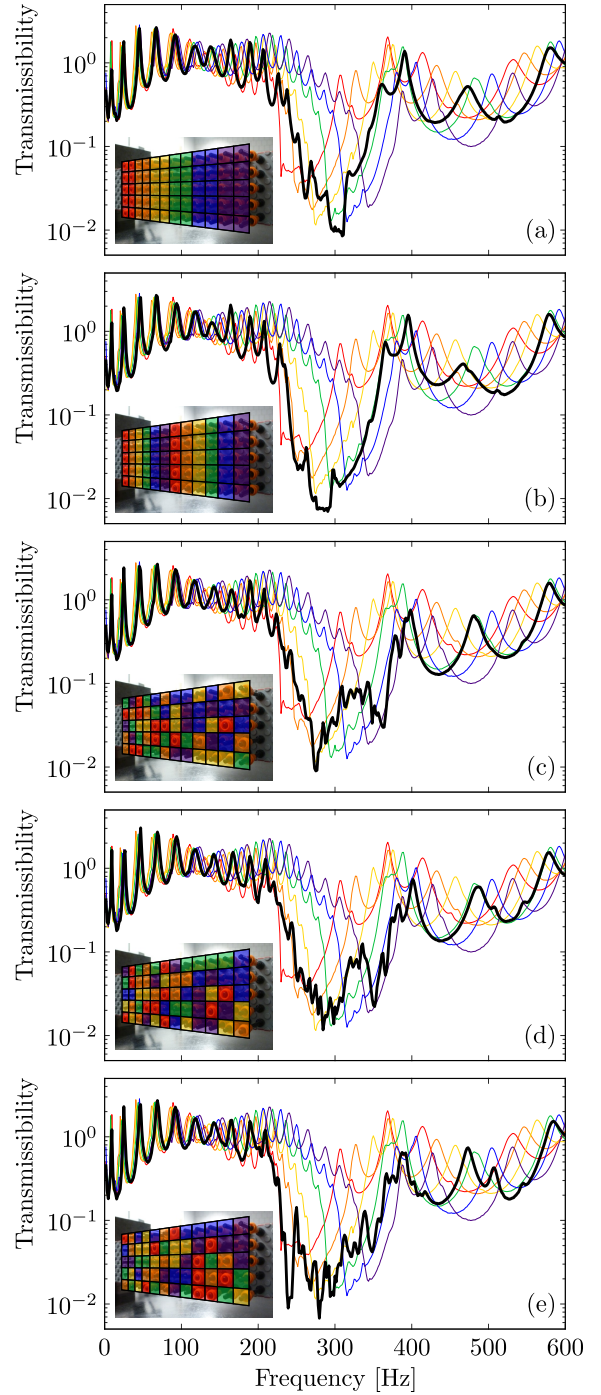


FIGURE 3: Influence of the spatial arrangement of heterogeneously tuned resonators on wave attenuation. In all cases, 10/60 resonators are programmed according to each of the brick configurations shown in Fig. 1b. (a), (b) Transmissibilities for functionally graded and (c), (d), (e) spatially randomized configurations, marked by thick black lines; thin color-coded lines refer to uniformly tuned monochromatic configurations (see color coding in Fig. 1b).

thick black line represents the transmissibility of the configuration depicted in the corresponding insert (all the ar-

chitectures feature 10 resonators of each kind—T, M1, M2, M3, M4, M5; the color coding is shown in Fig. 1b). The thin colored lines, used as reference, are the transmissibilities measured using six uniform arrangements, each featuring 60 identically tuned resonators; these spectra illustrate that resonators are tuned as to display partially overlapping bandgaps [32]. The results for two functionally-graded architectures with different gradient periodicity are compared in Figs. 3a-b and clearly highlight a widening of the bandgap with respect to their monochromatic counterpart, consistently with the rainbow trapping paradigm [12–14]. In both cases, the total bandgap spans the frequency region occupied by the individual gaps of the M1, M2, M3 monochromatic configurations (from the onset of the orange gap to the end of the green gap), and, interestingly, displays a shape that conforms to that of the individual gaps (sharp onset and sloping end). We also notice that the configuration in Fig. 3b produces a wider and deeper gap than the one in Fig. 3a—which suggests that the performance of functionally graded architectures can be corrected by modifying the period of the spatial arrangement. The results for three distinct *disordered* arrangements (involving the same resonators used in Figs. 3a-b) are shown in Figs. 3c-e. We immediately notice that the morphological characteristics of the bandgaps present additional features compared to the functionally graded cases—namely a “jagged” profile and a reduced attenuation within certain frequency bands inside the gaps. More importantly, the bandgaps are found to be systematically wider than their counterparts observed in ordered configurations—spanning here the frequency regions occupied by four/five (instead of three) individual bandgaps. Similar conclusions can be reached by working with other heterogeneous configurations [32]. Both the presence of resonant peaks inside the bandgap and the widening of the bandgap are consistent with observations reported for a number of systems featuring “transmission gaps” and exhibiting Anderson localization effects [36–39]. These results are unique in that the bandgap widening manifestation typical of Anderson localization is here triggered by superimposing spatial disorder onto a system that is initially ordered, yet inherently aperiodic by virtue of heterogeneity.

It has been demonstrated by Lemoult et al. that sub-wavelength waveguiding and localization can be obtained in locally-resonant acoustic and electromagnetic metamaterials by introducing defects featuring up-shifted resonators [7]. The phenomenon can be explained invoking Fano-type interference mechanisms, whereby a resonator impinged upon by an incident wave stores energy and re-radiates it into the medium; if the frequency of the incoming wave is slightly larger than its resonance, incoming and re-radiated waves have opposite phase and destructively interfere, causing the opening of a subwavelength bandgap (which in fact begins at resonance and ends when the amplitude of the resonator spectrum drops); at frequencies right before resonance, on the other hand, incoming and

re-radiated waves interact constructively. When placing an up-shifted resonator within a host medium in bandgap mode, waves tend to localize near the outlier due to the local availability of constructive interference—while destructive interferences bar them from propagating elsewhere; this results in waveguiding or localization depending on the arrangement of the resonators. This behavior, unlike that observed in systems with vacancy-like defects and empty waveguides [19, 24, 40, 41], is not limited to scenarios where the wavelength is significantly larger than the characteristic size of the defect (or the width of the waveguide). To date, only few theoretical studies have addressed subwavelength waveguiding in elastic media [42, 43], and these phenomena still beg for experimental evidence.

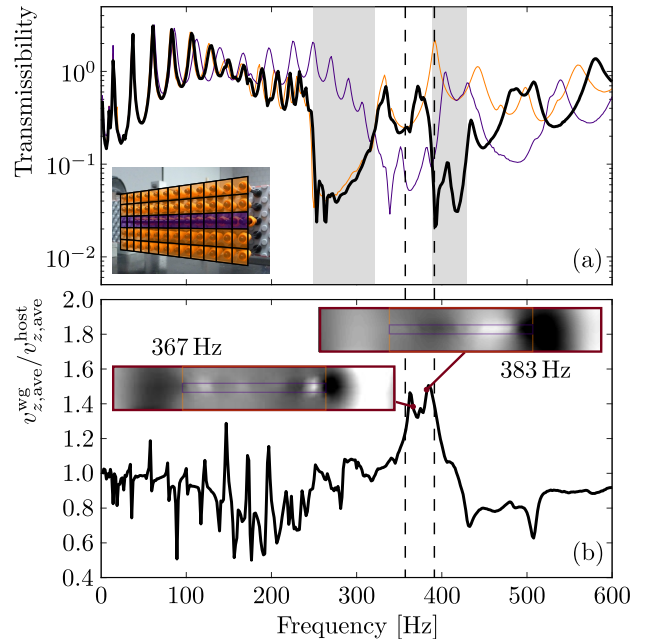


FIGURE 4: Subwavelength waveguide (obtained via a line of M5 resonators in M1 host). (a) Transmissibility (solid line refers to the configuration in the insert; colored lines show the reference cases of uniformly tuned M1 and M5 configurations). (b) Amplitude ratio between measurements at points of the plate inside the waveguide and points in the brick-populated area. The inserts show out-of-plane velocity wavefields capturing localization along the path of the waveguide (color-coded thin lines bound regions occupied by the corresponding brick type).

The thick line in Fig. 4a represents the transmissibility of a configuration featuring a horizontal line of up-shifted M5 resonators within a M1 host architecture. The underlying orange and purple lines represent the transmissibilities of uniform architectures with 5×12 M1 and M5 resonators, respectively. The response of the waveguide specimen follows the profile of the M1 bandgap between approximately 245 Hz and 325 Hz; this attenuation region is followed by a transmission zone, which extends until 385 Hz (near the end of the bandgap of the configuration with all M5 resonators), and by another bandgap, ranging from 385 Hz to 435 Hz. It

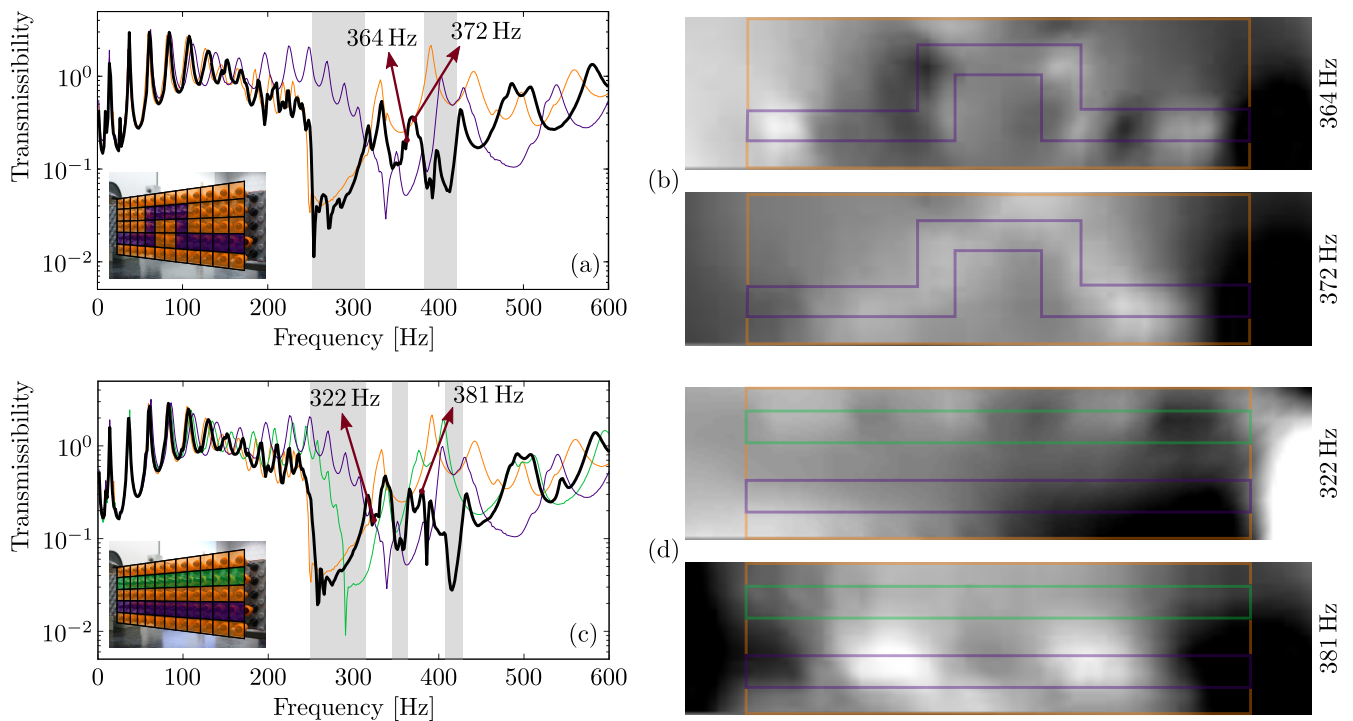


FIGURE 5: (a) Ω -shaped waveguide (M1 host, M5 waveguide). (c) Frequency selective waveguide (M1 host, M3 and M5 waveguides). (b), (d) Out-of-plane velocity wavefields at selected frequencies for configurations in (a) and (c), respectively. Note that, to better visualize the waveguiding behavior, the thresholding is customary to each wavefield frame.

is not surprising that the presence of a waveguide causes the appearance of a transmission region—as also documented in the literature [7, 10]. What is more surprising is that this transmission region is not located inside, but rather right above the frequency interval of the bandgap obtained with the uniform M1 population. Moreover, the waveguide specimen features a second bandgap which, albeit possessing the same morphological characteristics as that of the M5 configuration, is “pushed-up” towards higher frequencies (it begins roughly where the bandgap of the up-shifted population ends). These observations somehow elude the rationale that successfully described acoustic up-shifting mechanisms in [7]. To prove that the presence of the up-shifted resonators causes the arising of subwavelength localization mechanisms, in Fig. 4b, we plot the ratio between the average out-of-plane velocity measured at points of the plate inside the waveguide ($v_{z,\text{ave}}^{\text{wg}}$), and that measured inside the surrounding region populated by M1 bricks ($v_{z,\text{ave}}^{\text{host}}$). The plot has a peak plateau confined approximately between 360 Hz and 395 Hz. This interval corresponds to a subset of the transmission region observed in Fig. 4a. The standing wavefields reported as inserts in Fig. 4b for selected frequencies inside the interval show localization along the waveguide. Although the wording is still object of debate [44], it is reasonable to characterize these as subwavelength waveguiding effects since the wavelength of the standing wave (λ) in the bare plate is almost one order of magnitude larger than the width of the guide (w_{wg}): $\lambda/w_{\text{wg}} \approx 9$.

To show the robustness of these observations, we report

the results obtained for two other waveguiding scenarios. First we consider the architecture in Fig. 5a, which features a Ω -shaped waveguide of M5 resonators in a M1 host. The transmissibility shows a behavior similar to that of the straight waveguide. Another interesting case is the frequency-selective waveguide shown in Fig. 5c, partially inspired by the computational work of Guo et al. [45], where it is shown that a functionally graded array of stubs (where the gradient runs perpendicular to the direction of wave propagation) on a semi-infinite medium behaves as a multi-channel filter: at some frequencies, waves propagate only along a single channel but not along the others. A simplified version of their device can be realized on a stubbed plate by selecting a common host and two separate waveguides consisting of resonators with different resonant frequencies (here, as shown in Fig. 5c, we placed M3 and M5 resonators in the two waveguides). The transmissibility plot now features three bandgaps and two transmission regions. In Fig. 5d, we can see that waves propagate along the M3 waveguide when we operate in the first transmission region (at 322 Hz), while they travel along the M5 waveguide when we excite in the second transmission region (at 381 Hz). We conclude that, at different frequencies, waves can selectively propagate along different channels.

In this letter, we have shown that the design space of mechanical metamaterials—to date predominantly limited to ordered, uniform or graded architectures—can be enhanced by simultaneously leveraging heterogeneous populations of resonators and establishing degrees of organized disorder

in the microstructure. In particular, we have shown that bandgap widening can be attained via disordered spatial arrangements of heterogeneous resonators tuned at adjacent frequencies. We have also provided a first body of experimental evidence for subwavelength localization of elastic waves, and reported on a bandgap “push-up” effect in the transmissibility of elastic systems with up-shifted resonators.

SG and PC acknowledge the support of the National Science Foundation (grant CMMI-1266089). PC acknowledges the support of the University of Minnesota through the Doctoral Dissertation Fellowship. We thank Weiting Zhang and Nathan Bausman for their assistance and for helpful discussions, Mugurel Turos for helping with the setup, and Kai Sun of the University of Michigan for fruitful discussions.

-
- [1] Z. Liu, X. Zhang, Y. Mao, Y. Y. Zhu, Z. Yang, C. T. Chan, and P. Sheng, *Science* **289**, 1734 (2000).
- [2] H. Zhu and F. Semperlotti, *Phys. Rev. Lett.* **117**, 034302 (2016).
- [3] A.-C. Hladky-Hennion, J. O. Vasseur, G. Haw, C. Cronne, L. Haumesser, and A. N. Norris, *Appl. Phys. Lett.* **102**, 144103 (2013).
- [4] S. Zhang, C. Xia, and N. Fang, *Phys. Rev. Lett.* **106**, 024301 (2011).
- [5] J. Zhu, J. Christensen, J. Jung, L. Martin-Moreno, X. Yin, L. Fok, X. Zhang, and F. J. Garcia-Vidal, *Nat. Phys.* **7**, 52 (2011).
- [6] K. L. Tsakmakidis, A. D. Boardman, and O. Hess, *Nature* **450**, 397 (2007).
- [7] F. Lemoult, N. Kaina, M. Fink, and G. Lerosey, *Nat. Phys.* **9**, 55 (2013).
- [8] M. Addouche, M. A. Al-Lethawe, A. Elayouch, and A. Khelif, *AIP Adv.* **4**, 124303 (2014).
- [9] Z. Gao, F. Gao, and B. Zhang, *Appl. Phys. Lett.* **108**, 041105 (2016).
- [10] N. Kaina, A. Causier, Y. Bourlier, M. Fink, T. Berthelot, and G. Lerosey, *arXiv:1604.08117v1* (2016).
- [11] J. Zhu, Y. Chen, X. Zhu, F. J. Garcia-Vidal, X. Yin, W. Zhang, and X. Zhang, *Sci. Rep.* **3**, 1728 (2013).
- [12] S. Krödel, N. Thomé, and C. Daraio, *Extreme Mech. Lett.* **4**, 111 (2015).
- [13] D.-G. Zhao, Y. Li, and X.-F. Zhu, *Sci. Rep.* **5**, 9376 (2015).
- [14] D. Cardella, P. Celli, and S. Gonella, *Smart Mater. Struct.* **25**, 085017 (2016).
- [15] Z. Tian and L. Yu, *Sci. Rep.* **7**, 40004 (2017).
- [16] T.-T. Wu, Z.-G. Huang, T.-C. Tsai, and T.-C. Wu, *Appl. Phys. Lett.* **93**, 111902 (2008).
- [17] Y. Pennec, B. Djafari-Rouhani, H. Larabi, J. O. Vasseur, and A. C. Hladky-Hennion, *Phys. Rev. B* **78**, 104105 (2008).
- [18] M. Oudich, M. Senesi, M. B. Assouar, M. Ruzenne, J.-H. Sun, B. Vincent, Z. Hou, and T.-T. Wu, *Phys. Rev. B* **84**, 165136 (2011).
- [19] M. B. Assouar, M. Senesi, M. Oudich, M. Ruzzene, and Z. Hou, *Appl. Phys. Lett.* **101**, 173505 (2012).
- [20] F. Casadei, T. Delpero, A. Bergamini, P. Ermanni, and M. Ruzzene, *J. Appl. Phys.* **112**, 064902 (2012).
- [21] Y. Achaoui, V. Laude, S. Benchabane, and A. Khelif, *J. Appl. Phys.* **114**, 104503 (2013).
- [22] M. Rupin, F. Lemoult, G. Lerosey, and P. Roux, *Phys. Rev. Lett.* **112**, 234301 (2014).
- [23] R. Pourabolghasem, A. Khelif, S. Mohammadi, A. A. Eftekhar, and A. Adibi, *J. Appl. Phys.* **116**, 013514 (2014).
- [24] P. Celli and S. Gonella, *Appl. Phys. Lett.* **107**, 081901 (2015).
- [25] P. W. Anderson, *Phys. Rev.* **109**, 1492 (1958).
- [26] Z. Wu, R. L. Harne, and K. W. Wang, *J. Intel. Mat. Syst. Struct.* **27**, 1189 (2016).
- [27] S. Lee, B. Kang, H. Keum, N. Ahmed, J. A. Rogers, P. M. Ferreira, S. Kim, and B. Min, *Sci. Rep.* **6**, 27621 (2016).
- [28] G. Memoli, M. Caleap, M. Asakawa, D. R. Sahoo, B. W. Drinkwater, and S. Subramanian, *Nat. Commun.* **8**, 14608 (2017).
- [29] C. Goffaux and J. P. Vigneron, *Phys. Rev. B* **64**, 075118 (2001).
- [30] V. Romero-García, C. Lagarrigue, J.-P. Groby, O. Ri-choux, and V. Tournat, *J. Phys. D: Appl. Phys.* **46**, 305108 (2013).
- [31] M. Thota, S. Li, and K. W. Wang, *Phys. Rev. B* **95**, 064307 (2017).
- [32] See supplemental material (in tail of this document) for a more detailed account on the experimental setup and for additional results.
- [33] O. R. Bilal and M. I. Hussein, *Appl. Phys. Lett.* **103**, 111901 (2013).

- [34] E. Coffy, T. Lavergne, M. Addouche, S. Euphrasie, P. Vairac, and A. Khelif, *J. Appl. Phys.* **118**, 214902 (2015).
- [35] J. H. Oh, H. M. Seung, and Y. Y. Kim, *Appl. Phys. Lett.* **108**, 093501 (2016).
- [36] O. Thorp, M. Ruzzene, and A. Baz, *Smart Mater. Struct.* **10**, 979 (2001).
- [37] R. Sainidou, N. Stefanou, and A. Modinos, *Phys. Rev. Lett.* **94**, 205503 (2005).
- [38] C. H. Hodges, *J. Sound Vib.* **82**, 411 (1982).
- [39] J. A. Judge, B. H. Houston, D. M. Photiadis, and P. C. Herdic, *J. Sound Vib.* **290**, 1119 (2006).
- [40] M. Oudich, M. B. Assouar, and Z. Hou, *Appl. Phys. Lett.* **97**, 193503 (2010).
- [41] W. Jiang, D. Feng, D. Xu, B. Xiong, and Y. Wang, *Appl. Phys. Lett.* **109**, 161102 (2016).
- [42] M. Addouche, M. A. Al-Lethawe, A. Elayouch, and A. Khelif, *AIP Adv.* **4**, 124303 (2014).
- [43] A. A. Maznev and V. E. Gusev, *Phys. Rev. B* **92**, 115422 (2015).
- [44] A. A. Maznev, G. Gu, S. y. Sun, J. Xu, Y. Shen, N. Fang, and S. y. Zhang, *New J. Phys.* **17**, 042001 (2015).
- [45] Y. Guo, M. Hettich, and T. Dekorsy, *New J. Phys.* **19**, 013029 (2017).

Supplemental material (SM)

Details on the experimental setup

In this section, we provide some additional detail regarding our experimental setup. While in Fig. 2 we showed a schematic representation of it, a picture of our setup is shown in Fig. S1. The specimen (see also Fig. 1a) is made of

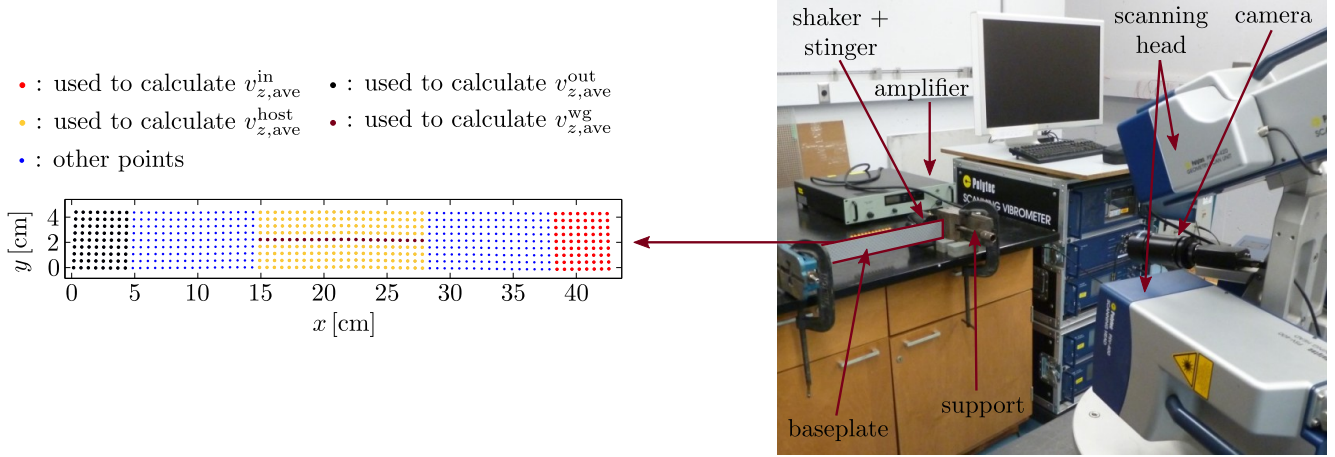


FIGURE S1: Picture of the experimental setup and detail of the scanning grid—that comprises those pre-defined points of the baseplate where the lasers perform the measurement. The legend illustrates which scanning points are used to calculate the quantities that are used to compute transmissibilities and relative motion plots.

a strip cut out from a gray acrylonitrile butadiene styrene (ABS) baseplate (LEGO[®], Item 10701) and features 12×5 telescopic resonators arranged in a square lattice architecture. The strip is 5.7 cm wide and the distance between the clamped ends is approximately 46.3 cm. Each resonator is characterized by a rod (LEGO[®], Elem. ID 395726) and a conical brick (LEGO[®], Elem. ID 4518029) in prismatic contact. The conical brick can be slid up and down the rod to tune the resonator’s natural frequency; the rod-brick contact is strong enough for the brick to hold its position throughout the tests. Note that the resonators are attached to the baseplate through frictional contact as well (anchoring the base of the rod to one of the protuberances—*studs*—of the baseplate). The standing wave excitation signals are transmitted to the structure through an electromechanical shaker (Brüel & Kjær Type 4810) and a stinger. The out of plane velocity time histories of points on the back-side of the plate belonging to the pre-determined grid shown in Fig. S1 are recorded via a 3D Scanning Laser Doppler Vibrometer (3D-SLDV, Polytec PSV-400-3D). The acquisition is performed in the frequency domain (the Fast Fourier Transform is performed automatically within the PSV acquisition system). To eliminate non-repeatable noisy features from the response, measurements are repeated 10 times and averaged at each measurement location. As far as the vibrometer channel is concerned, we select a 5 V range and DC coupling. We acquire in the 0–5 kHz frequency range, and we concentrate on the 0–600 Hz band when postprocessing the data. The sampling frequency is $f_s = 12.8$ kHz and the number of FFT lines is 3200, resulting in a frequency resolution of 1.5625 Hz. The selected velocity decoder is the digital VD-08-10 mm/s/V, that allows acquisitions up to 20 kHz. The excitation is a pseudorandom waveform with maximum amplitude of 500 mV. The excitation signal is amplified using a Brüel & Kjær Type 2718 Power Amplifier, with gain set to 30 dB.

Throughout this work, we used two different setups, featuring the same specimen but slightly different boundary conditions (due to the fact that it is nearly impossible to clamp the specimen exactly the same way twice): the first setup is used throughout the bandgap analysis, while the second one is used for the subwavelength localization experiments. Inevitably, the two setups are characterized by a slightly different response; while the bandgap onset associated with a specific type of resonator is unaffected by changes in the boundary conditions, other characteristics such as the bandgap profile and the resonant peaks of the structure will be altered. The transmissibilities of the specimen for both setups, displaying several uniform resonator configurations, are shown in Fig. S2. Fig. S2a represents the response of the first setup, the one used throughout the bandgap analysis. The colored lines correspond to different configurations, as shown in the legend (Fig. S2c). It is interesting to see how the dips in the transmissibilities are only due to the presence of the bricks, as highlighted by the almost-flat response of the specimen without bricks (gray line). We can also appreciate how the resonators are tuned at adjacent frequencies, as displayed by the fact that their bandgaps are overlapping. Similar considerations can be made for the second setup, the one used for the wave localization experiments, whose response is shown in Fig. S2b.

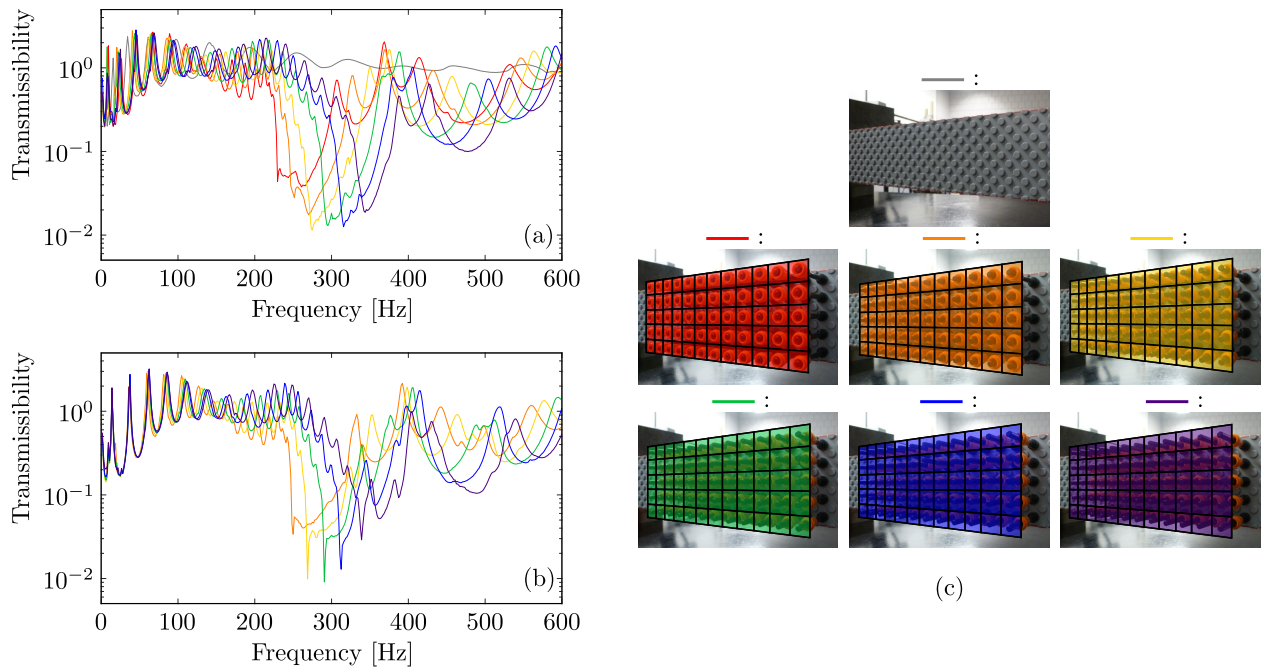


FIGURE S2: (a), (b) Comparison between the transmissibilities of configurations featuring uniform arrangements of 5×12 bricks. The two sets of results differ slightly in terms of boundary conditions of the specimen. (c) Legend, showing the brick arrangement corresponding to each of the lines in (a), (b). Superimposed to the bricks is a grid composed of squares colored according to the color code introduced in Fig. 1b (to better distinguish different brick configurations).

Our specimens are extremely flexible and are made of a polymeric material. To rule out nonlinearities from our explanations, we decided to investigate whether our specimens present any signature of nonlinearity in their response. In order to address this issue, we compared the responses of the same architecture featuring only M1 resonators to excitations at different amplitudes. The transmissibility plots for three loading amplitudes (0.1 V, 0.5 V—the amplitude used for all experiments throughout this letter—and 1.0 V) are superimposed in Fig. S3. We can see that the only

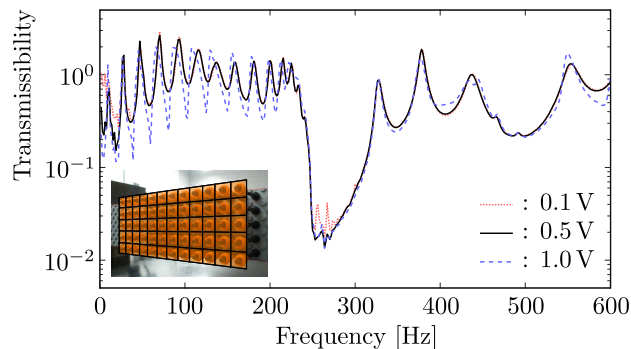


FIGURE S3: Response of a uniform M1 architecture to three different loading amplitudes.

difference between the 0.1 V case and the 0.5 V case is represented by the morphology of the bandgap—with the 0.1 V case being characterized by a jagged “bottom”. With respect to the other two cases, the high amplitude (1.0 V) one is characterized by a different response both before and after the bandgap. We believe this amplitude-dependent behavior to be indeed due to a mix of material and geometric nonlinearities that are triggered when the load is larger than a certain threshold. However, we exclude that nonlinearities affect our observations on bandgap widening, due to the fact that the amplitude of excitation does not significantly affect the extent of the bandgap, whose sharp onset and sloping end are unchanged.

More on broadband wave attenuation

In this section, we report additional results related to the attenuation capabilities of architectures featuring functionally-graded and disordered spatial arrangements. In the letter, we reported on various architectures displaying 10 resonators of each of the following types: T, M1, M2, M3, M4, M5. In Fig. S4, we show that similar considerations can be made for architectures comprising 15 M1, 15 M2, 15 M3 and 15 M4 resonators. We can see that bandgaps for the functionally

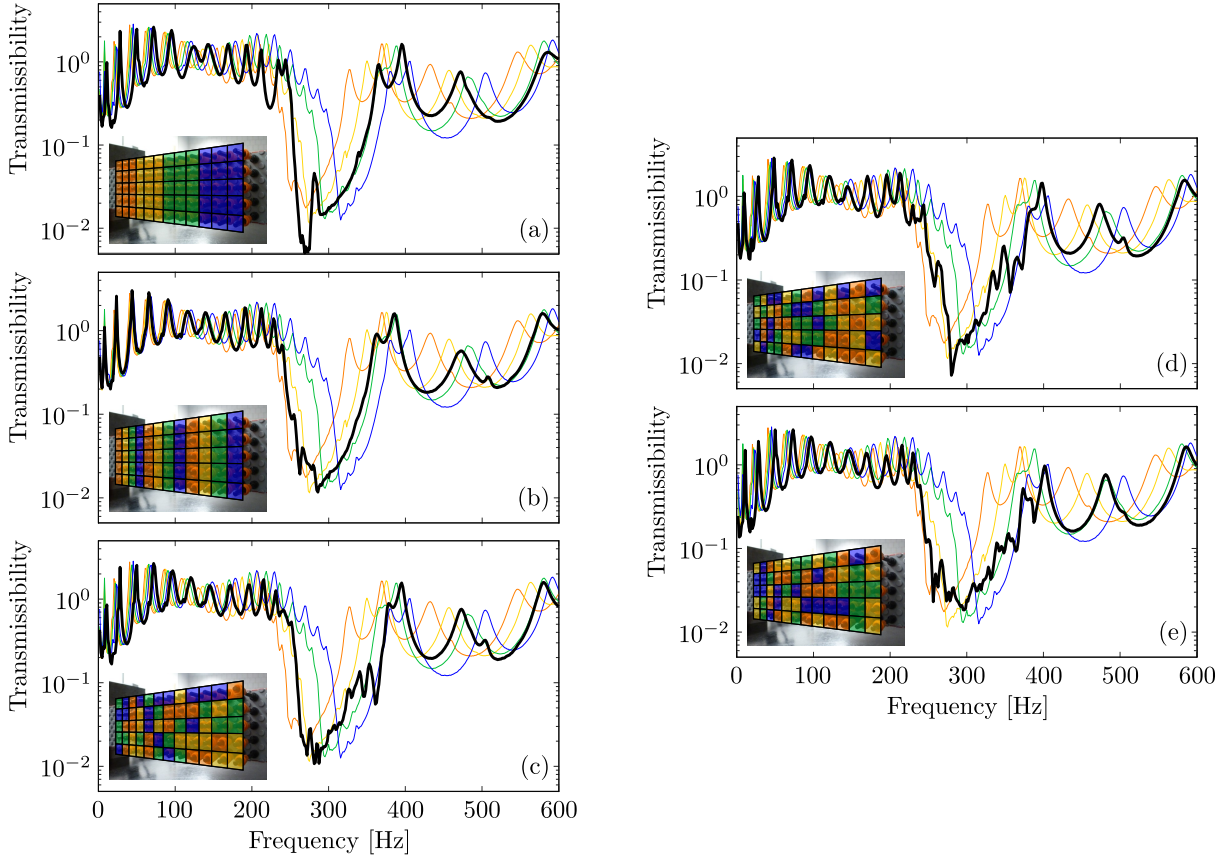


FIGURE S4: Influence of the spatial arrangement of heterogeneously tuned resonators on wave attenuation. In all cases, 10/60 resonators are programmed to the brick configurations M1, M2, M3 and M4. (a), (b) Transmissibilities for functionally graded and (c), (d), (e) spatially randomized configurations, marked by thick black lines; thin color-coded lines refer to uniformly tuned monochromatic configurations (see color coding in Fig. 1b).

graded architectures, shown in Figs. S4a-b, span two of the reference bandgaps (yellow and green) and present a similar morphology (sharp onset and sloping end). On the other hand, the bandgaps of configurations featuring disordered brick arrangements are wider than their graded counterparts, spanning three or four individual bandgaps as shown in Figs. S4c-e, and also present different morphological characteristics (they have a “jagged” profile, while also being less deep).

In Fig. S5, we show the response of architectures comprising 30 M1 and 30 M2 resonators. As we decrease the degree of heterogeneity among resonator characteristics, we can see that the results for functionally-graded and disordered architectures do not differ much. Even though it is challenging to make qualitative comments about bandgap width, we are able to see that the bandgaps in Figs. S5a-b are more regular than those in Figs. S5c-e.

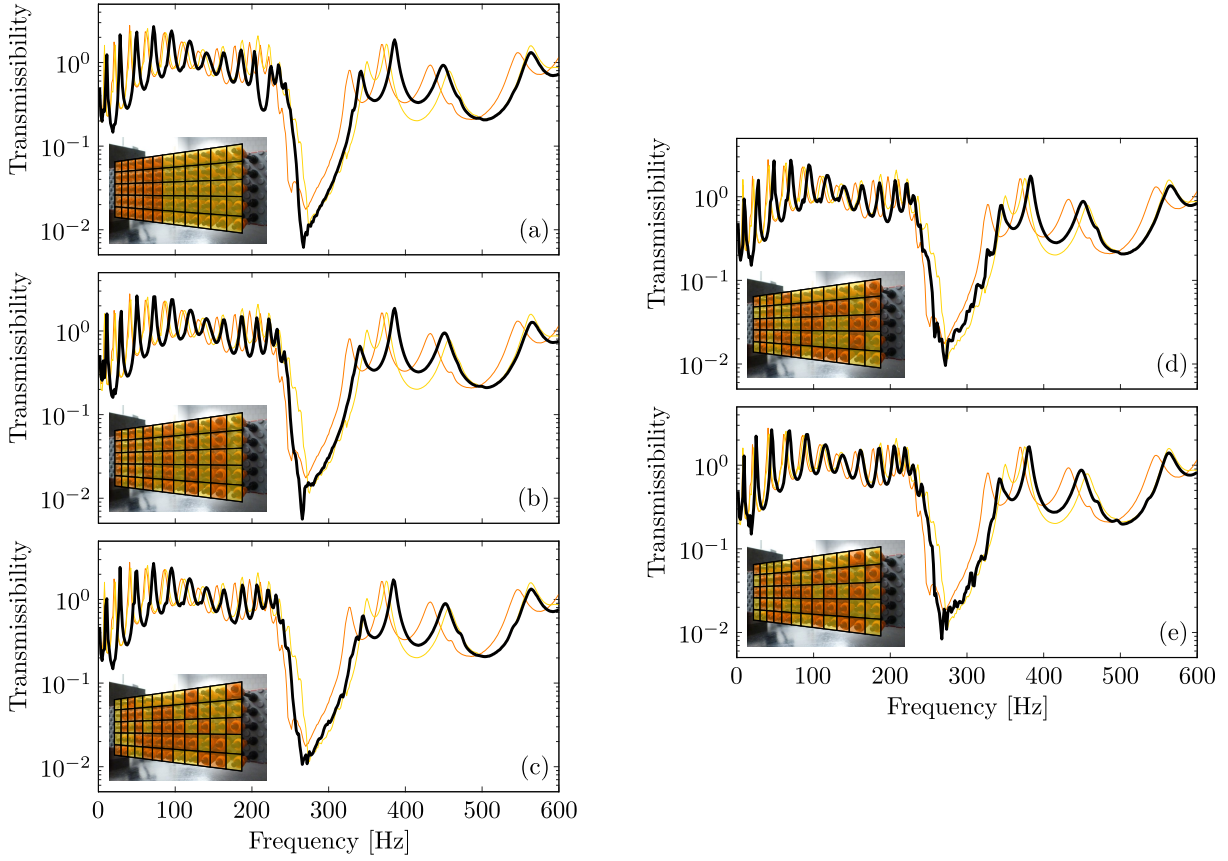


FIGURE S5: Influence of the spatial arrangement of heterogeneously tuned resonators on wave attenuation. In all cases, 30/60 resonators are programmed to the brick configurations M1, M2. (a), (b) Transmissibilities for functionally graded and (c), (d), (e) spatially randomized configurations, marked by thick black lines; thin color-coded lines refer to uniformly tuned monochromatic configurations (see color coding in Fig. 1b).

More on subwavelength localization

In this section, we show additional results in terms of wave localization and confinement that complement those reported in the letter. We begin by showing once again, for the sake of convenience, the results obtained for a straight M5 waveguide in a M1 host. These are shown in Figs. S6a-b. As discussed in the letter, we can see that the presence of

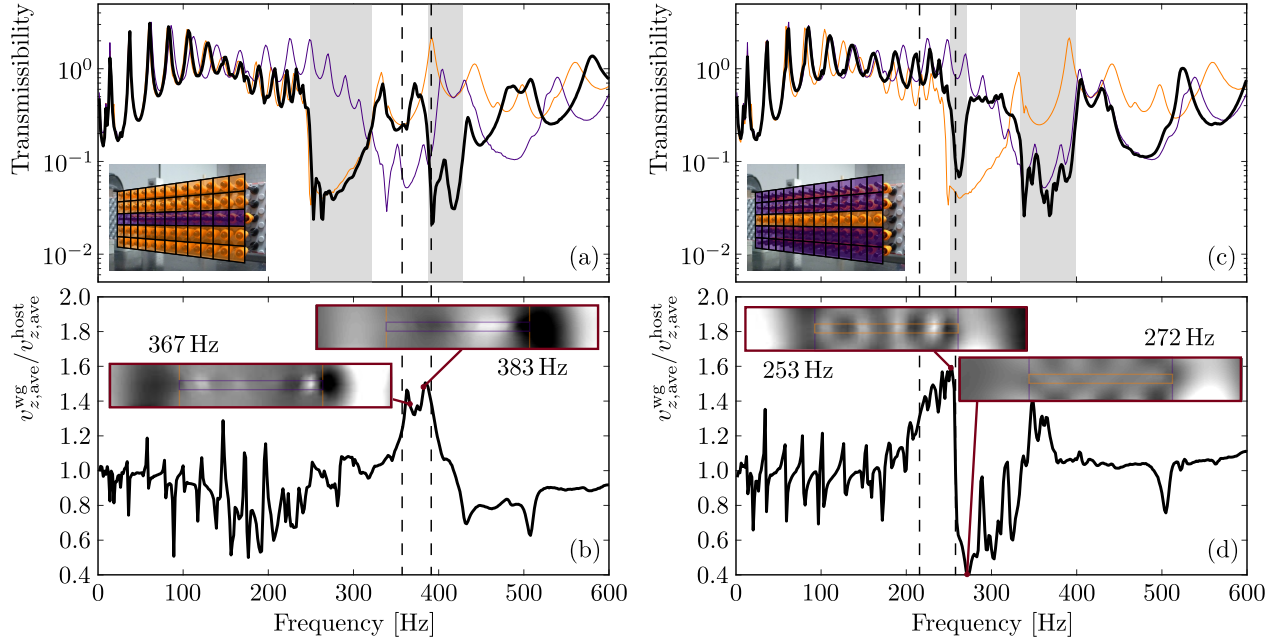


FIGURE S6: (a) Straight waveguide (obtained via a line of M5 resonators in M1 host). (c) Reversed straight waveguide (obtained via a line of M1 resonators in M5 host). (b), (d) Amplitude ratios between measurements at points of the plate inside the waveguide and points in the brick-populated area, for the configurations in (a) and (c), respectively. The inserts show out-of-plane velocity wavefields capturing localization along the path of the waveguide (color-coded thin lines bound regions occupied by the corresponding brick type).

the up-shifted resonators causes the appearance of a transmission region right after the end of the bandgap of the host architecture (M1) and extending up until the end of the bandgap of the M5 architecture. From the amplitude ratio plot in Fig. S6b, we can see that only a sub-portion of the transmission region is characterized by wave localization within the waveguide. This result is intriguing, yet counterintuitive if interpreted through a standard subwavelength waveguiding formalism. In light of Lemoult et al. [F. Lemoult, N. Kaina, M. Fink, and G. Lerosey, *Nat. Phys.* **9**, 55 (2013)], we should expect the transmission region to be located before the beginning of the bandgap of the M5 resonators—when the incoming waves interfere constructively with the ones re-radiated by the M5 resonators. On the other hand, we observe that, clearly, this subwavelength localization behavior takes place well within the M5 bandgap. The other odd aspect is represented by the appearance of a second bandgap in the transmissibility: this gap looks similar to the one of the M5 architecture (see the double dip structure where the first one is a sharp dip and the second is a rounded one), but is pushed up in frequency—beginning when the M5 gap ends. We believe this effect to be something germane to the problem of elastic waves in stubbed plates, and to require additional investigation.

To attempt an interpretation of this behavior, we report the results obtained using other waveguides. In Figs. S6c-d, we show the complementary case to that discussed above: a M1 waveguide in a M5 host. We can see that the transmissibility presents features similar to those of the M5-in-M1 case: we have two bandgaps and a transmission region in between. The first gap begins with the one of the M1 architecture, and ends shortly afterwards, when the M1 gap reaches its bottom. The second gap is similar to the one of the M5 architecture. The amplitude ratio plot in Fig. S6d, on the other hand, shows a radically different scenario with respect to the one in Fig. S6b. Here, we can see that we have very strong localization up until the beginning of the first gap—as also highlighted by the wavefield at 253 Hz—and after the beginning of the M5 bandgap. On the other hand, in the transmission region from 276 Hz to 328 Hz, we see a dip in the amplitude ratio, which highlights how the amplitude recorded in the brick region outside the waveguide is much larger than the amplitude recorded within the waveguide. This “reverse” waveguide behavior is visible in the wavefield at 272 Hz. It is interesting to note that the behavior of this M1-in-M5 specimen can be partially explained with the formalism of Lemoult et al.: we see localization within the waveguide before the bandgap of M1 because of the constructive wave interference between the M1 bricks and the plate; within the transmission region, from 276 Hz to

328 Hz, we see localization outside the waveguide due to the constructive interference between incoming waves and those re-radiated by the M5 bricks. Still, this formalism does not seem to explain the second localization peak occurring after the beginning of the M5 gap.

Our investigation continues with the analysis of other waveguide architectures characterized by a M1 host. The results for an empty waveguide are reported in Figs. S7a-b. Fig. S7a highlights how the introduction of an empty waveguide

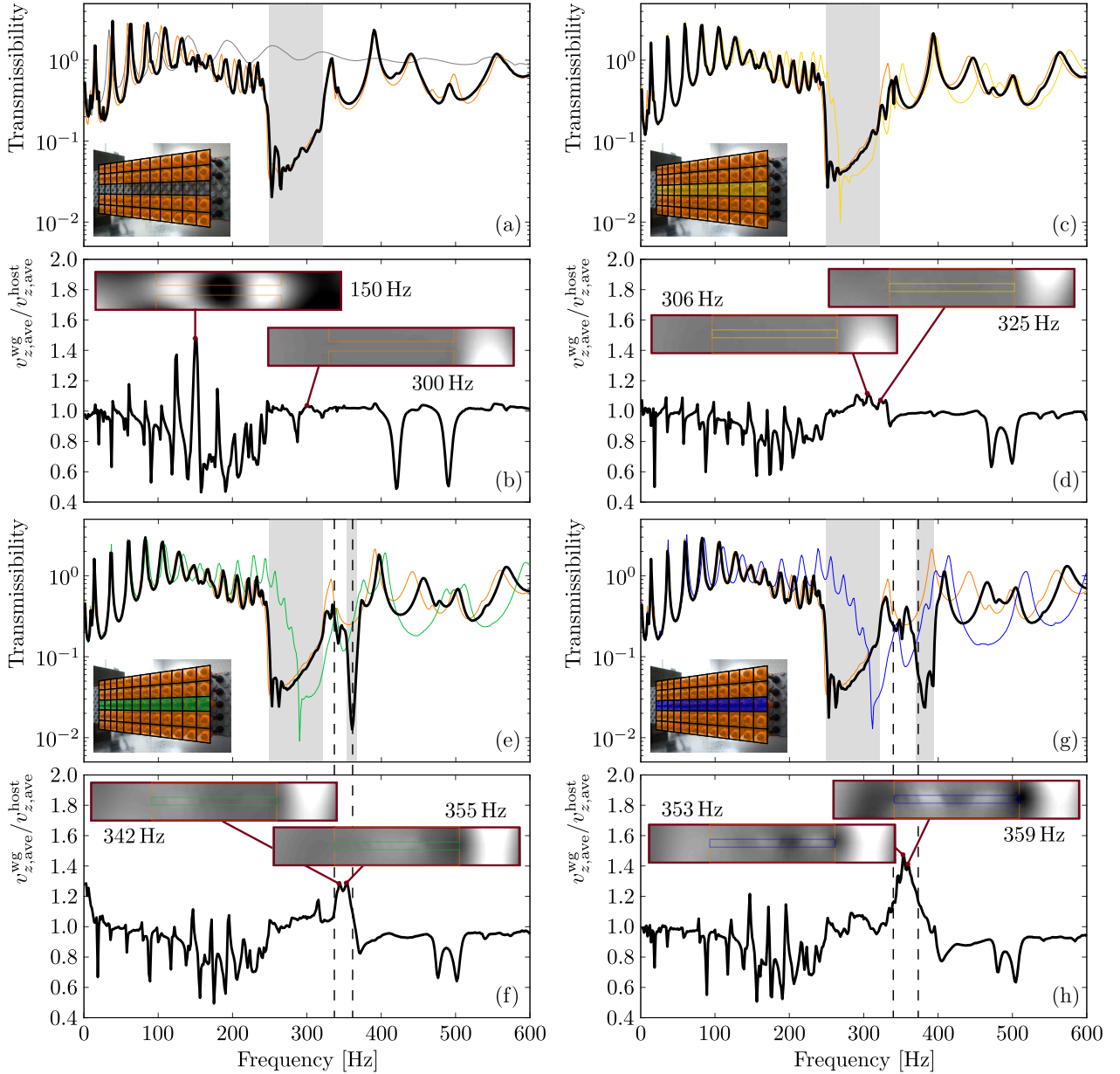


FIGURE S7: (a), (c), (e), (g) Straight waveguides (featuring a M1 host and empty, M2, M3, M4 lines of defects, respectively). (b), (d), (f), (h) Amplitude ratios between measurements at points of the plate inside the waveguide and points in the brick-populated area, for the configurations in (a) and (c), (e), (g), respectively. The inserts show out-of-plane velocity wavefields capturing localization along the path of the waveguide (color-coded thin lines bound regions occupied by the corresponding brick type).

does not produce significant effects from a transmissibility standpoint. This is also visible from the amplitude ratio plot in Fig. S7b, which does not present any interesting feature in the neighborhood of the bandgap. Note that the sharp peak at 150 Hz is not associated with a true localization within the waveguide, as highlighted by the corresponding wavefield. The presence of M2 resonators within the path of defects, as shown in Figs. S7c-d is still not enough to produce localization effects. Things change when we place M3 resonators within the waveguide, as shown in Figs. S7e-f. These up-shifted resonators clearly impact the transmissibility plot, where we record the appearance of a transmission

region following the M1 bandgap and followed by a second thin gap, which extends up to the end of the M3 gap. Note that the structure seen in this transmissibility plot is analogous to that observed for the M5-in-M1 waveguide. In the M3 case, however, we clearly see that the waveguiding behavior is weaker than the one observed in Figs. S6a-b. Similar considerations apply to the M4-in-M1 waveguide, whose response (shown in Figs. S7g-h) is characterized by a stronger waveguiding, albeit still less pronounced than the M5-in-M1 case. In light of these results, we can conclude that not all up-shifted resonators produce localization effects. As the resonant frequency of the up-shifted resonators grows larger, the localization effects increase in intensity (note that we did not consider resonators with resonant frequencies larger than that of M5). We can also conclude that localization effects are always accompanied by a peculiar transmissibility plot featuring two bandgaps (the one of the host medium and a “pushed-up” one) and a transmission region in between (localization only occurs within a sub-region of this transmission region).

While, up to this point, we only discussed waveguiding scenarios, similar considerations apply to point defects. In general, these defects produce small effects on the transmissibility of the architecture, while affecting the wavefields in a macroscopic way. This is shown in Figs. S8a-b for a M5-in-M1 point defect. In analogy with the frequency-selective waveguide discussed in the letter, we here report the response of a frequency-selective point defect (Figs. S8c-d). In Fig. S8d, the wavefields at 372 Hz and 381 Hz show localization around the M5 defect, while the one at 333 Hz is characterized by a (mild) localization around the M3 resonator.

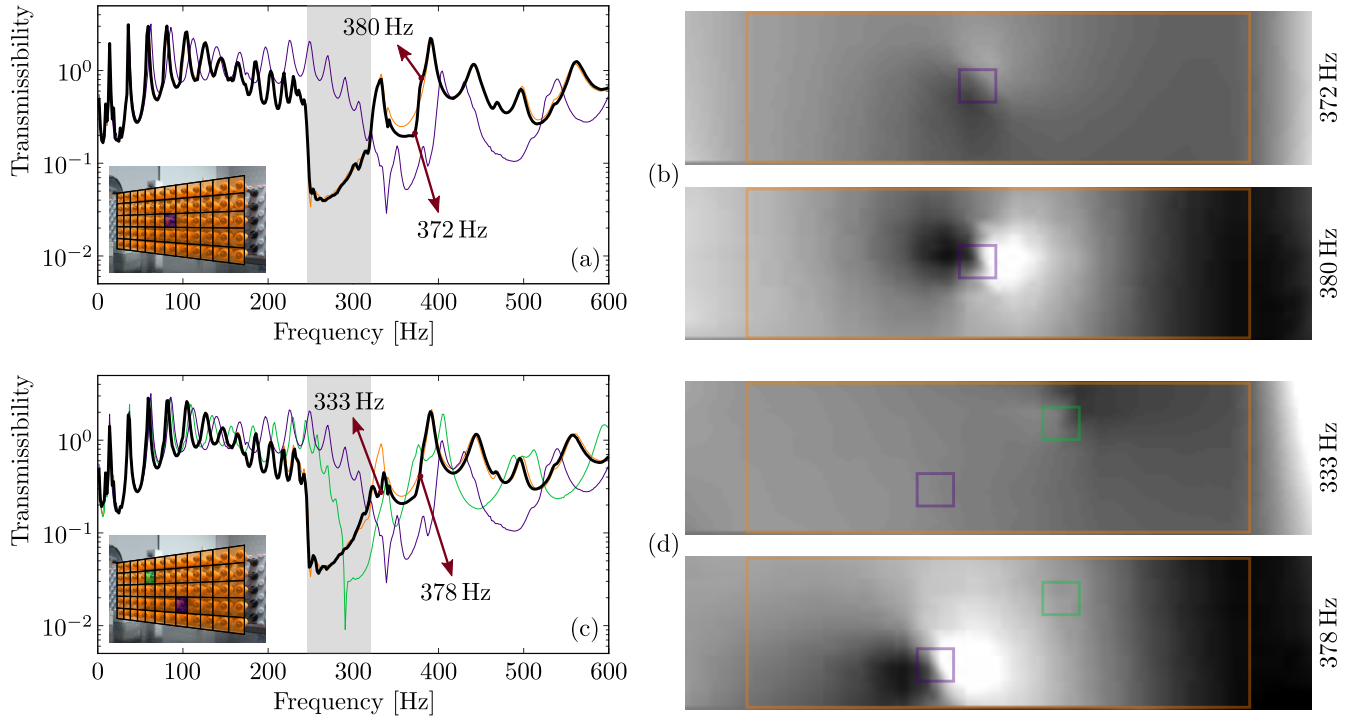


FIGURE S8: Wave Localization. (a) Single M5 defect in host of M1 resonators. (c) Frequency-selective defect (M1 host featuring one M3 and one M5 defects). (b), (d) Out-of-plane velocity wavefields at selected frequencies for configurations in (a) and (c), respectively. Note that, to better visualize the waveguiding behavior, the thresholding is customary to each wavefield frame.